Applied Catalysis B: Environmental 221 (2018) 9–16

Contents lists available at ScienceDirect

Applied Catalysis B: Environmental

journal homepage: www.elsevier.com/locate/apcatb

Research Paper

Oxygen-doped nanoporous carbon nitride *via* water-based homogeneous supramolecular assembly for photocatalytic hydrogen evolution

Jing-Wen Zhang[a,b], Si Gong[a,b], Nasir Mahmood[a,b], Lun Pan[a,b], Xiangwen Zhang[a,b], Ji-Jun Zou[a,b,*]

[a] Key Laboratory for Green Chemical Technology of the Ministry of Education, School of Chemical Engineering and Technology, Tianjin University, Tianjin, 300072, China
[b] Collaborative Innovative Center of Chemical Science and Engineering (Tianjin), Tianjin, 300072, China

ARTICLE INFO

Keywords:
Carbon nitride
Photocatalysis
Supramolecular assembly
Oxygen-doping
Hydrogen evolution

ABSTRACT

Graphitic carbon nitride (g-C_3N_4) has emerged as a promising photocatalyst, but poor charge separation and low surface area limit its activity. Here, we report a hydrothermal method to generate hydrogen bonded supramolecular complex *via* water-based homogeneous supramolecular assembly, which is a promising precursor to fabricate porous and oxygen-doped g-C_3N_4. The hydrothermal treatment provides a homogeneous environment for hydrolysis of melamine to produce cyanuric acid and reaction of cyanuric acid with remained melamine to create the in-plane ordering and hydrogen bonded supramolecular complex. The complex can template uniform nanoporous structure and also provide an opportunity for O-doping in the g-C_3N_4 network upon calcination in air. The resulted g-C_3N_4(GCN-4) possesses high surface area, well-defined 3D morphology and oxygen-dopant in the lattice. Subsequently, the visible light absorption, charge separation, and wettability are considerably enhanced. This catalyst exhibits higher hydrogen evolution rate by 11.3 times than the bulk g-C_3N_4 under visible light irradiation, with apparent quantum efficiency of 10.3% at 420 nm.

1. Introduction

Graphitic carbon nitride (g-C_3N_4) has attracted widespread attention in photocatalytic hydrogen evolution and environmental remediation as a promising metal-free and visible-light-responsive photocatalyst [1–3]. However, high recombination rate of charge carriers, low surface area and low electrical conductivity limit the activity of g-C_3N_4 synthesized by traditional methods, which can be improved by controlling the morphology, electronic and optical properties through nanostructuring, heteroatom doping and copolymerization [4–6]. In particular, simultaneous utilization of nanostructure design, high porosity and heteroatom doping such as oxygen can increase the active surface area and optimize the electronic structure to broaden light-absorption and effective charge separation. Porous g-C_3N_4 can be fabricated by soft templating method where organic directing agents lead the pore formation but need to be eliminated at the end. As well, hard templating uses ordered 2D or 3D porous solid materials and requires harsh conditions to remove the template to achieve final product [7–19]. In contrast to conventional templating strategies, supramolecular preorganization approach provides an easy control over structure by assembling monomers into supramolecular aggregates *via* hydrogen bonding. Through calcination, the removal of hydrogen bonds results in higher degree of freedom and yields well-organized 3D porous network, while it does not require any external template [1,20]. Along with the good control over morphology, the supramolecular complex strategy also provides an opportunity to tune the electronic structure through the doping of suitable heteroatoms.

Thus, extensive research has been carried out on the development of nanostructured g-C_3N_4 materials through supramolecular preorganization by linking melamine with triazine derivatives like cyanuric acid and trithiocyanuric acid to produce hydrogen-bonded molecular assemblies [20–24]. The solvent plays a crucial role in the preorganization process, because it can influence the equilibrium geometry and dynamic behavior of the monomers [23,25,26]. However, melamine and cyanuric acid are just slightly dissolvable in most solvents at room temperature, thus it is impossible to provide a homogeneous chemical reaction environment. Till now, dimethylsulphoxide and chloroform have been explored as the solvent to produce ordered hydrogen-bonded supramolecular structures because of their capability to dissolve melamine and cyanuric acid, but their use is not environmentally friendly [25,27]. On the other hand, nonmetal heteroatom doping can modify the local electronic structure which can enhance the visible light harvesting capability, charge separation efficiency and thus photocatalytic activity. Specially, oxygen can play more effective role in this regard

* Corresponding author at: Key Laboratory for Green Chemical Technology of the Ministry of Education, School of Chemical Engineering and Technology, Tianjin University, Tianjin, 300072, China.
E-mail address: jj_zou@tju.edu.cn (J.-J. Zou).

http://dx.doi.org/10.1016/j.apcatb.2017.09.003
Received 18 May 2017; Received in revised form 28 July 2017; Accepted 2 September 2017
Available online 05 September 2017
0926-3373/

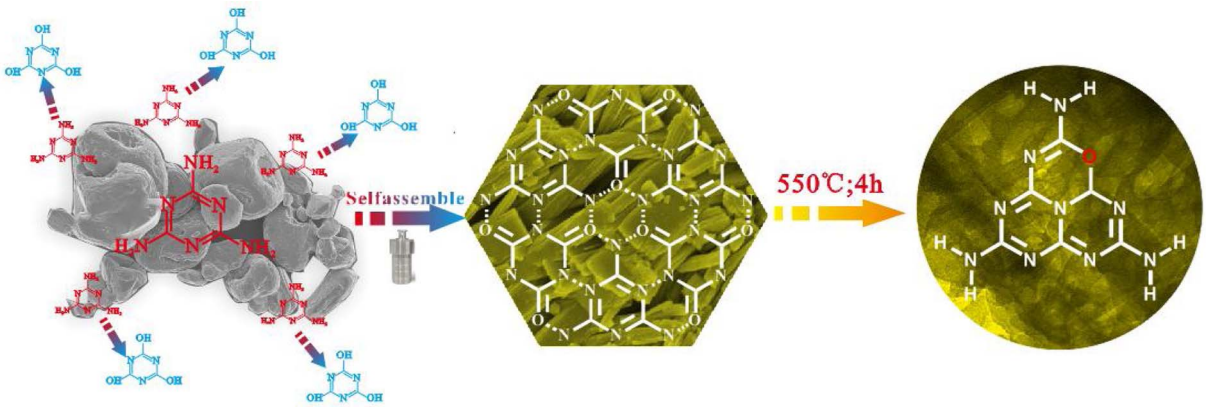

Scheme 1. Illustration of fabrication of O-doped porous g-C_3N_4 from hydrogen bond-induced supramolecular precursor assembled under hydrothermal treatment.

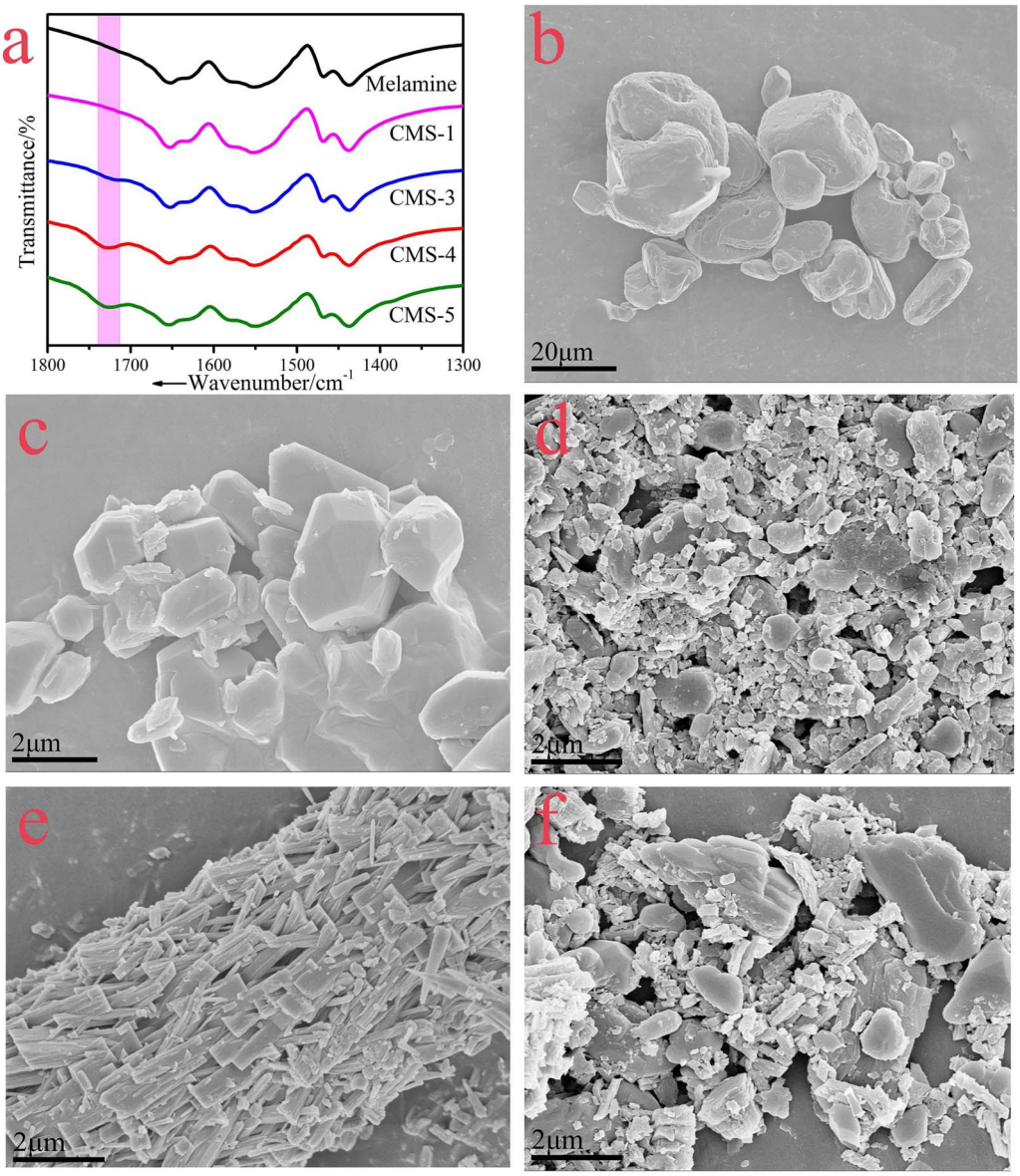

Fig. 1. a) FTIR spectra of pristine-melamine and CMS. The SEM images of (b) pristine melamine, (c) CMS-1, (d) CMS-3, (e) CMS-4 and (f) CMS-5.

[28–35]. Oxygen-doped g-C_3N_4 have been synthesized by treating g-C_3N_4 with H_2O_2 or under oxygenated atmosphere, and treating melamine with H_2O_2 to be the precursor [28–34]. But these strategies do not provide easy control on structure, especially for the later one, because such treatment is a heterogeneous solid-liquid reaction, which limit the formation of hydrogen bonds on the surface of melamine that may induce inhomogeneity and limited bonding [29]. So we aim to search an environmentally benign and cheap solvent that can dissolve melamine,

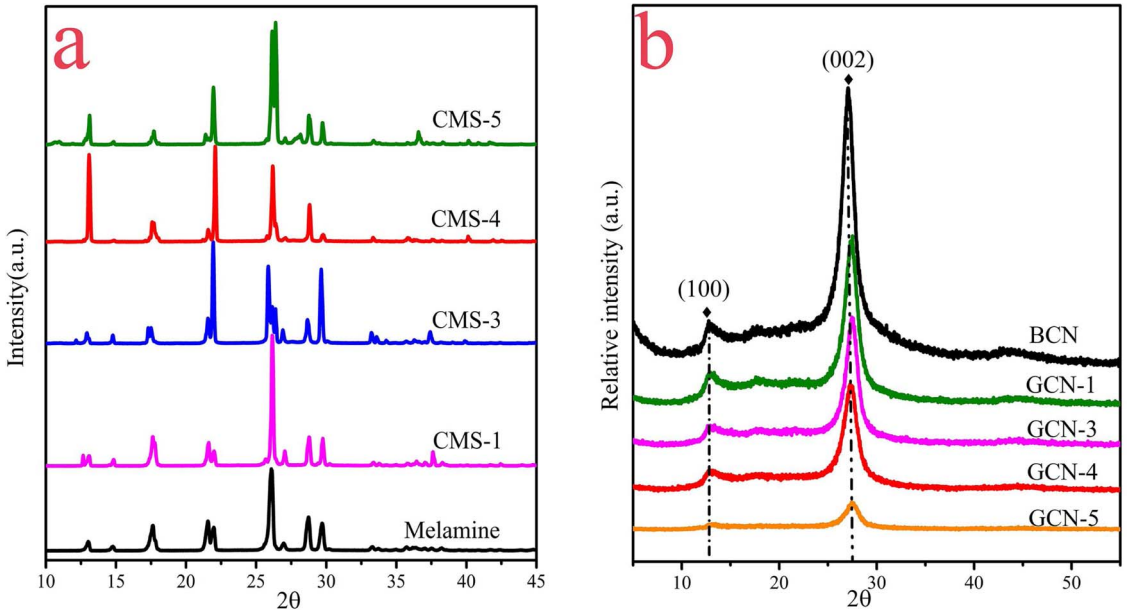

Fig. 2. a) XRD pattern of pristine-melamine and CMS; b) XRD pattern of bulk g-C_3N_4 and GCN.

thus providing opportunity to construct the supramolecular complexes as precursor of highly porous g-C_3N_4 nanostructures and introduce heteroatoms at the same time.

Herein, we present an efficient and ecofriendly hydrothermal treatment of melamine to synthesize supramolecular precursor that is then transferred to O-doped porous g-C_3N_4 (Scheme 1). The hydrothermal treatment in water ensures full dissolution of melamine and provides a homogeneous environment for supramolecular assembly to form a well-ordered in-plane and hydrogen-bonded cyanuric acid-melamine supramolecular complex. On calcination, O-doped g-C_3N_4 with three-dimensional pore architecture is obtained. The resulted g-C_3N_4 has much improved activity of about 11.3 times higher than pristine C_3N_4 in photocatalytic hydrogen evolution reaction (HER) under visible light irradiation, achieving an apparent quantum efficiency of 10.3% at 420 nm.

2. Experimental section

2.1. Fabrication of carbon nitride

Melamine was purchased from Aladdin Industry Corporation. Milli-Q ultra-pure water with a resistivity higher than 18.2 MΩ·cm was used in all experiments. All the chemicals were reagent grade and used as received. In a typical synthesis, 3 g of melamine were added in 40 mL water under continuous magnetic stirring. After 30-min stirring, the mixture was transferred into a 50 mL Teflon-lined stainless-steel autoclave, sealed and heated at 200 °C under continuous magnetic stirring of 100 r/min for different time (x = 1, 3, 4, and 5 h). Then the white precipitates were filtered and washed with water and ethanol for several times, and dried at 60 °C overnight. The resulting powders (labelled as CMS-x) were calcined in air at 550 °C for 4 h with heating rate of 2.3 °C/min, and the final samples were labelled as GCN-x. The yield of CMS from melamine is 85 ~ 90%, and the yield of C_3N_4 from CMS is 30 ~ 40%. As reference, bulk g-C_3N_4 was synthesized by calcining melamine at 550 °C for 4 h according to literatures and labelled as BCN [34].

2.2. Characterizations

XRD patterns were recorded using D/MAX-2500 X-ray diffractometer equipped with Cu Kα radiation at 40 kV and 140 mA at a scanning rate of 5°/min. SEM images were observed using a field-emission scanning electron microscope (Hitachi, S-4800). High resolution TEM (HR-TEM) analysis was carried out using a Tecnai G2 F-20 transmission electron microscope with a field-emission gun operating at 200 kV. X-ray photoelectron spectrum (XPS) analysis was conducted with a PHI-1600 X-ray photoelectron spectroscope equipped with Al Kα radiation, and the binding energy was calibrated by the C1 s peak (284.8 eV) of contamination carbon. Time-resolved anisotropy decays were recorded on a FL3 system (Horiba Scientific, Edison, NJ) utilizing time-correlated single photon count. Steady-state photoluminescence (PL) spectra were measured by a Horiba JobinYvon Fluorolog 3–21 with the excitation light at 375 nm. Specific surface area and pore size distribution were calculated based on N_2 adsorption/desorption isotherms conducted on Micromeritics TriStar 3000 at 77 K, all samples were outgassed under vacuum at 300 °C for 4 h. UV–vis diffuse reflectance spectra (UV-vis DRS) were obtained from a Hitachi U-3010 spectrometer equipped with a 60 mm diameter integrating sphere using $BaSO_4$ as reference. Water contact angle was measured with OCA 15EC video-based contact angle goniometer (Data Physics, Germany) by the sessile drop method.

2.3. Photocatalytic hydrogen evolution

Photocatalytic hydrogen evolution was carried out in a closed Pyrex top-irradiation vessel (280 mL). Typically, 50 mg of catalyst were dispersed in an aqueous solution (120 mL) containing triethanolamine (10 vol%) as electron donor. Co-catalyst (3 wt% Pt) was introduced by in-situ photodeposition. The reaction solution was evacuated several times to completely remove air prior to irradiation and then filled with Argon to 101 kPa. The reaction was conducted under a 300 W Xeon-lamp equipped with a 420 nm-cut-off filter, and the temperature was maintained at 0 °C. The evolved gas was analyzed by gas chromatography equipped with a thermal conductive detector (TCD) and a 5 Å molecular sieve column, using nitrogen gas as the carrier gas.

The apparent quantum efficiency (AQE) was measured using the same experimental setup. The irradiation area was controlled as 20 cm^2. The intensity was measured using a UV-A radiometer (Photoelectric Instrument Factory, Beijing Normal University, model UV-A). For 400, 420, 450, 500, 550 and 600 nm monochromatic light, the intensity was 4.31, 7.56, 11.09, 15.49, 10.86, and 20.28 mW/cm^2 respectively. Using the amount of hydrogen produced in an average of

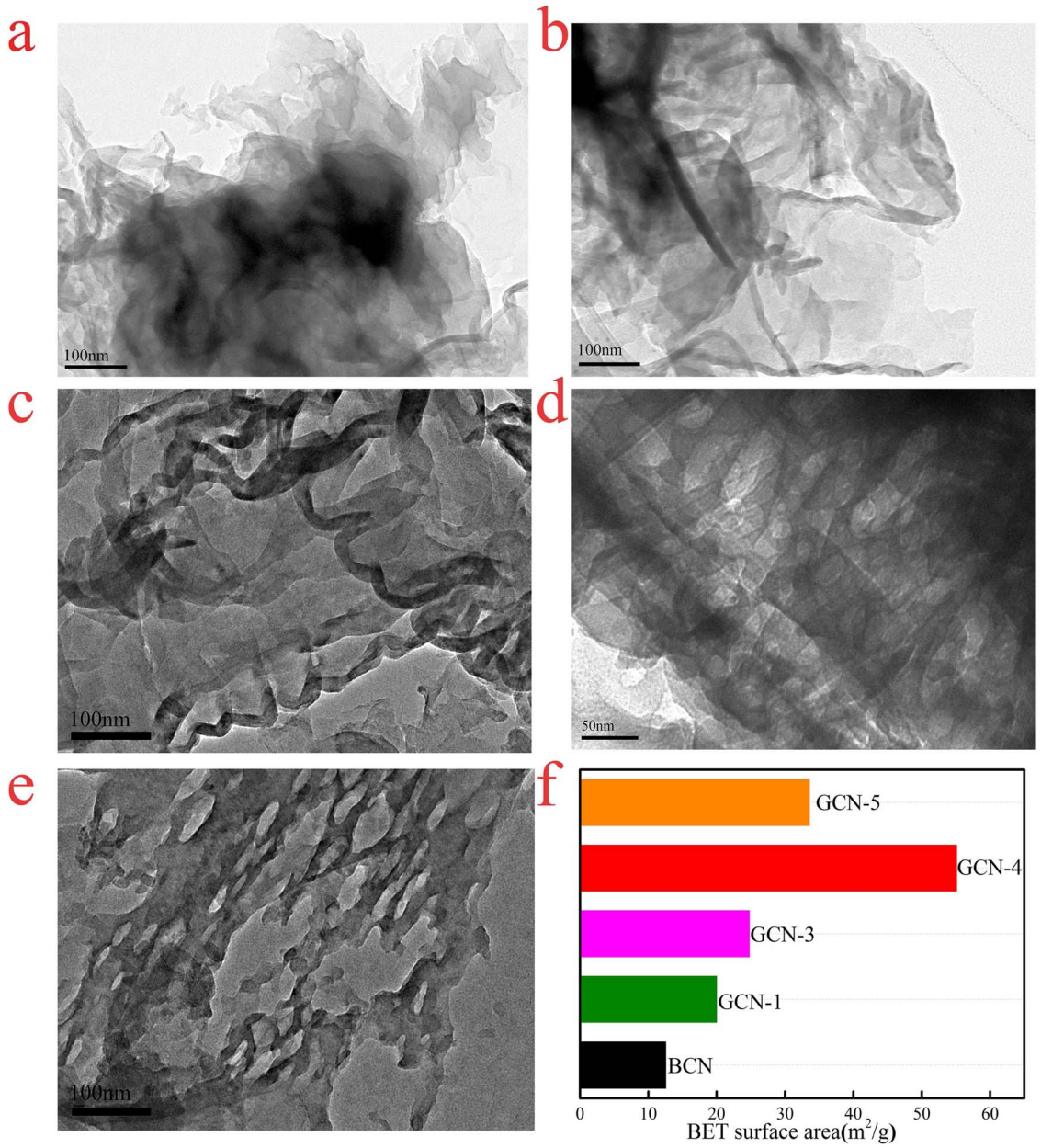

Fig. 3. TEM images of (a) bulk g-C_3N_4, (b) GCN-1, (c) GCN-3, (d) GCN-4 and (e) GCN-5; f) BET surface area of bulk g-C_3N_4 and GCN.

one hour (total reaction time is 3 h), the AQY was calculated as AQY = *Ne/Np* × 100%, where *Ne* is the amount of reaction electrons, *Np* is the amount of incident photons.

2.4. Photoelectrochemical measurements

The electrochemical and photoelectric properties were performed on a CHI 660 B electrochemical system (Shanghai, China) using a standard three-electrode cell with a working electrode, a platinum wire counter electrode, and an Ag/AgCl reference electrode. Na_2SO_4 (0.2 M) was used as the electrolyte solution. The working electrode was prepared by dip-coating photocatalyst slurry on an F-doped tin oxide (FTO) glass electrode (1 × 1.5 cm^2) and heating it at 40 °C overnight. All the investigated working electrodes were of similar thickness. Electrochemical impedance spectroscopy (EIS) measurements were carried out with a sinusoidal ac perturbation of 10 mV applied over the frequency range of 0.01–10^5 Hz.

3. Results and discussion

Typically, at room temperature melamine is slightly soluble in water, however high temperature and pressure can increase its solubility. Therefore, melamine is fully dissolved in water under hydrothermal treatment, which can be hydrolyzed into cyanuric acid. Under suitable conditions, the cyanuric acid molecules start reacting with non-hydrolyzed melamine molecules to form a well-ordered in-plane and hydrogen-bonded cyanuric acid-melamine supramolecular (CMS) complex as illustrated in Scheme 1. The direct evidence for the formation of CMS complexes comes from the FT-IR spectra, shown in Fig. 1a and S1. The newly formed hydrogen bonds are reflected by the appearance of additional peak at ~1720 cm^{-1} corresponding to the stretching vibrational mode of C═O [36]. This peak appears after 3 h's hydrothermal treatment and becomes stronger with the increasing hydrothermal time, indicative of the increased degree of hydrolysis and self-assembly of monomeric sub-units (Fig. 1a). Correspondingly, in Fig. S1 the peaks at 3469 and 3420 cm^{-1} (NH_2 stretching vibrations), 337

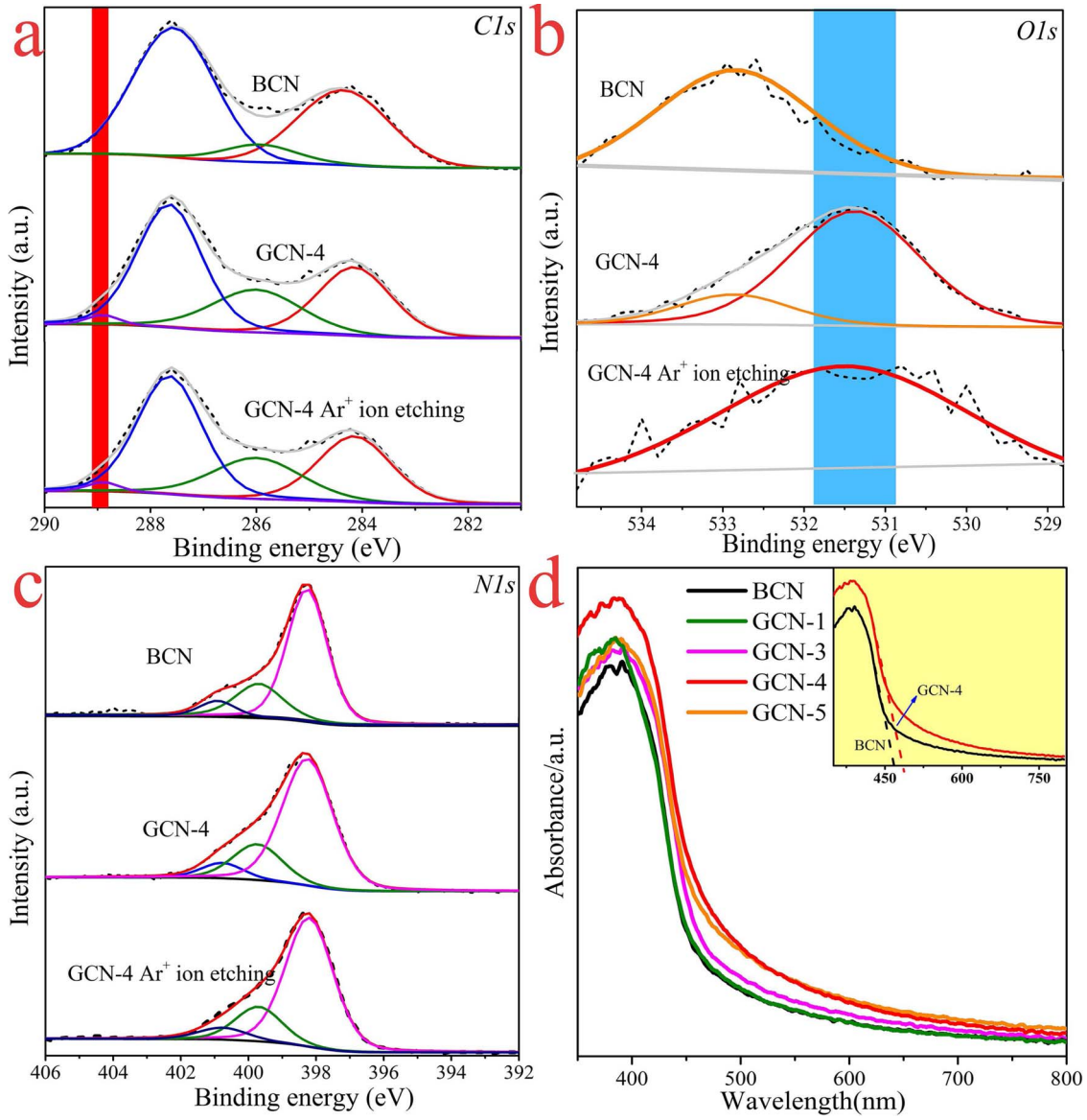

Fig. 4. Devolution of a) C1s, b) O1 s and c) N1 s XPS spectra of GCN-4 and bulk g-C_3N_4; d) UV–vis absorption spectra of bulk g-C_3N_4 and GCN.

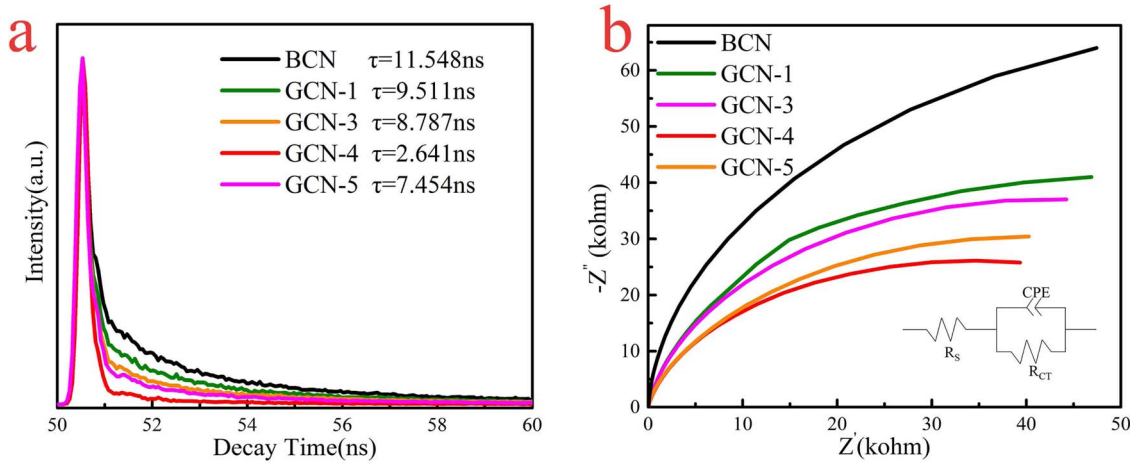

Fig. 5. a) The fitting curves of fluorescence decay of bulk g-C_3N_4 and GCN (excitation at 375 nm); b) EIS spectra of BCN and GCN in the dark.

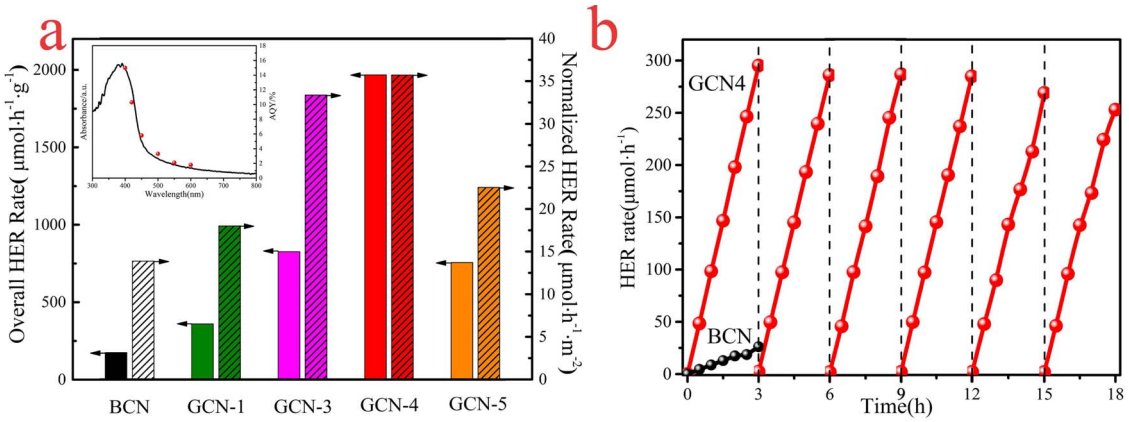

Fig. 6. (a) Overall and Normalized HER rate of bulk g-C_3N_4 and GCN, and wavelength-dependent AQY of GCN-4 (inset); (b) Cycling HER of GCN-4 under visible-light irradiation ($\lambda > 420$ nm).

and 3137 cm^{-1} (asymmetric and symmetric stretching absorptions of N—H), 1654 cm^{-1} (deformation vibrations of N—H) and 1030 cm^{-1} (C—N stretching vibration) of CMS complexes are weakened compared with melamine, suggesting many N—H groups are transformed to —OH groups of cyanuric acids which then form hydrogen bonds with $-NH_2$ in the self-assembly process [21,25].

Scanning electron microscopy (SEM) images in Fig. 1b–f show the morphological aspects of pristine melamine and CMS complexes. Pristine melamine particle possesses irregular shape with size ranging from ten to hundreds of micrometers. While the CMS complexes bears smaller size that further decreases as the hydrothermal time increases, due to larger production of cyanuric acid by the increased hydrolysis of melamine. Interestingly, CMS-4 has the most uniform rods-like morphology with smooth surface, with an average diameter of ~300 nm and a length of ~1.5 μm. However, further increase in the hydrothermal time results in big and shapeless aggregation of CMS-5, possibly due to the excessive degree of hydrolysis which causes irregular assembly. In short, the well-dissolution of melamine in the water under high pressure and temperature provides an opportunity for molecular level construction of functional materials with controlled growth.

Further, to observe the crystalline structure of CMS complexes, the X-ray diffraction (XRD) patterns were recorded as shown in Fig. 2a. It is found that CMS complexes still possess the inherent structural features of melamine and show the typical diffraction peaks at 17.72°, 21.75°, 26.27°, and 28.87°, corresponding to (110), (012), (102), and (112) phases of melamine, respectively. So, it assures that the bulk crystalline structure of melamine doesn't change while arranging into various morphologies through hydrolysis and supramolecular complex formation. It is also worth mentioning that the peak at 12.8° corresponding to a hexagonal patterning gets stronger in CMS complexes, especially for CMS-4 and CMS-5, demonstrating the very improved in-plane order of the supramolecular complexes [37].

To produce g-C_3N_4 from CMS complexes, these CMS complexes were polymerized at 550 °C for 4 h under air. The crystalline structure and bonding situation of g-C_3N_4 are confirmed by XRD and FT-IR characterizations. As shown in Fig. 2b, the g-C_3N_4 nanosheets show two pronounced diffraction peaks with $2\theta = 13.2°$ and 27.4°, arising from the in-plane intervals of periodic tri-s-triazine units (100) plane and the interplanar stacking of aromatic systems (002) plane of graphite-like materials according to standard card JCPDS No. 87–1526. Notably the peak at 27.4° is weakened and broadened gradually from GCN-1 to GCN-5, confirming the breakage of interlayer framework and decreased thickness of nanosheets, as supported by the TEM images (Fig. 3a–e). The FT-IR spectra of g-C_3N_4 shows the feature of typical aromatic C—N heterocycle stretches at 1200–1700 cm^{-1} and the breathing mode of triazine units at 806 cm^{-1} (Fig. S4). The broad peak at 2900–3200 cm^{-1} is attributed to the N—H and O—H bands, associated with the residual uncondensed amino groups and the absorbed H_2O molecules, respectively [2].

The polymerization at high temperature removes the network of local hydrogen bonds in CMS complex and yields well-ordered 3D structure of g-C_3N_4. The SEM morphological studies show that bulk g-C_3N_4 bears the morphology of irregular agglomerated particles, while the resulted g-C_3N_4 from CMS complexes possess nanosheets 3D network with highly porous structure (Fig. S2). In particular, the submicrometer rod-like morphology of CMS-4 is well maintained during the polymerization. The resulted GCN-4 presents a relatively uniform and ordered nanoporous structure compared with g-C_3N_4 synthesized from other CMS complexes. To further reveal the morphology and porosity of g-C_3N_4, TEM studies were conducted as shown in Fig. 3. Fig. 3a shows that the bulk C_3N_4 is comprised of sheets which are densely packed in form of large particles without obvious porosity and ordering of structure. However, the g-C_3N_4 prepared from supramolecular complexes approach are comprised of thinner sheets with variable ordering and porosity (Fig. 3b–e). The sheets of GCN-1 (Fig. 3b) and GCN-3 (Fig. 3c) become thinner compared with bulk g-C_3N_4 but with lower degree of ordering, while GCN-4 shows obvious ordered nanoporous morphology (Fig. 3d). For GCN-5, the sheets are broken into small pieces due to removal of the large amount of hydrogen bonds in CMS-5 resulted from over hydrolysis of melamine. To verify the TEM results, the nitrogen adsorption-desorption measurements were carried (Fig. 3f and S3). The surface area increases from bulk g-C_3N_4 (12 $m^2 g^{-1}$) to GCN-1 (20 $m^2 g^{-1}$), GCN-3 (25 $m^2 g^{-1}$), and GCN-4 (55 $m^2 g^{-1}$), while decreases for GCN-5 (33 $m^2 g^{-1}$). High porosity can bring more hydrophilic surface as characterized by contact angle measurement (Fig. S5). All the GCN samples show smaller contact angle compared with bulk g-C_3N_4, and especially GCN-4 shows the smallest contact angle, indicating the best wettability which will then benefit the photocatalytic performance [38].

The elemental distribution and their nature were observed through EELS mapping and XPS analysis, which give the direct evidence of oxygen doping in g-C_3N_4. Fig. S6 shows the homogenous distribution of three elements (*i.e.* C, N, and O), which indicates the existence of oxygenated species in the planes of g-C_3N_4. But it's hard to declare that oxygen is doped in the planes. Thus, high resolution XPS spectra of C1s, O1s, and N1 s were recorded as shown in Fig. 4a–c, respectively. The C1 s spectra of bulk and oxygen doped porous g-C_3N_4 is fitted with two peaks *i.e.* one at 288.0 eV corresponding to the C—N—C coordination bond and the other peak at around 286.1 eV attributed to the C—NH_2 species in g-C_3N_4 [39]. Notably, a new peak at higher binding energy of 289.0 eV ascribed to the C—O bond appears in GCN [29]. Ar^+ etching was done to remove surface adsorbed oxygen, and interestingly this peak still exist (with area percentage of 3.4%), suggesting the formation of C—O bonds in-plane (Fig. 4a). Furthermore, in O1 s spectra the peak

appeared at 531.4 eV is ascribed to the C—O and N—C—O species in lattice of g-C_3N_4 (Fig. 4b) [30,31]. After Ar+ etching to remove the physically adsorbed oxygen and terminating oxidized groups, GCN still shows this peak with overall concentration of 1.63 mol%, confirming that O atoms are doped in the lattice planes of g-C_3N_4. On the contrary, bulk g-C_3N_4 does not show such oxygen signal of C—O or N—C—O, indicating the absence of oxygen dopants. Actually, our previous DFT calculation has proved that O atom can directly bond to sp2-hybridized carbon by substituting two-coordinated N atoms due to the extremely low formation energy [29], which is also in agreement with the case of S-doped g-C_3N_4 [40]. In addition, all the samples exhibit similar N1 s profiles with peaks at around 398.5, 399.8 and 401.0 eV which can be attributed to sp2-hybridized nitrogen (C—N-C), sp3-hybridized nitrogen (N-[C]3) and amino functional groups with a hydrogen atom (C—NH), respectively (Fig. 4c) [10,31].

It is noted that the oxygen doping can increase the visible light harvesting of g-C_3N_4 as shown in Fig. 4d. The absorption band edges of GCN are red-shifted compared with that of bulk g-C_3N_4, which is beneficial for visible light harvesting. In particular, the absorption edge of GCN-4 shifts to 481 nm corresponding to the band gap 2.58 eV compared to the bulk g-C_3N_4 (2.69 eV). The red shift of absorption edge comes from the alteration of electronic band structure due to the presence of O atom, since previous DFT calculation has illustrated that the band gap becomes narrower upon O-doping [29,30].

Along with the visible light harvesting capability, a good photocatalyst must have the ability to slow down the charge recombination. Therefore, time resolved fluorescence was measured to get the lifetime of charge carriers as shown in Fig. 5a. GCN have lower average fluorescence lifetime (2.641-9.511 ns) compared to the bulk g-C_3N_4 (11.548 ns), which is explained by the competition between fluorescence caused by charge recombination and charge separating channels. Decrease in luminescence indicates that the depopulation of the excited states occurs more easily through nonradiative pathways, which is considered as the charge transfer pathway leading to hydrogen generation [25,41,42]. So the reduced fluorescence lifetime indicates faster nonradiative recombination rate that means improved charge separation and transfer efficiency. The steady state photoluminescence (PL) measurements were also done (Fig. S7). The PL spectrum of bulk g-C_3N_4 emerges a strong emission peak at 460 nm originated from the band-to-band recombination of electrons and holes [28]. The intensity of this peak decreases dramatically for oxygen doped porous g-C_3N_4, especially for GCN-4, which means that the recombination of electrons and holes is effectively inhibited. Meanwhile, the shift to around 465 nm for emission peak of GCN-4 is consistent with the narrowed band gap due to oxygen doping (Fig. 4d). In accordance with the PL spectra, the arc radius of oxygen doped porous g-C_3N_4 in electrochemical impedance spectroscopy (EIS) Nyquist plot is smaller than that of bulk g-C_3N_4, suggesting the lowest resistance and fastest interfacial charge carrier transfer (Fig. 5b) [43–45].

The photocatalytic performance of bulk g-C_3N_4 and oxygen doped porous g-C_3N_4 was tested by calculating the hydrogen production under visible light. From Fig. 6a it is obvious that oxygen doped porous g-C_3N_4 shows an enhancement in the hydrogen evolution reaction by a factor of 2–11 over bulk g-C_3N_4 that shows a HER rate of 174 $\mu mol \cdot h^{-1} \cdot g^{-1}$ (normal rate according to previous literature) [1]. Especially, the HER rate of GCN-4 reaches 1968 $\mu mol \cdot h^{-1} \cdot g^{-1}$(with AQE of 10.3% at 420 nm), which is about 11.3-fold of bulk g-C_3N_4 and delivers a stable HER rate after 6 cycling trips (Fig. 6b). It is worth noting that the AQE of GCN-4 is better than most reported results (Table S1). Also, the wavelength-dependent quantum yield matches well with the UV–vis spectra (Fig. 6a inset), proving that the H_2 evolution of GCN-4 is strongly dependent on the wavelength of the incident light. Overall this enhanced photocatalytic activity of GCN-4 is originated from several factors such as (i) oxygen doping improves the charge separation and transfer efficiency as confirmed by PL and EIS characterizations, (ii) the ability of better light harvesting leads to more charge carriers in photocatalysis as confirmed by the wavelength-dependent quantum yield, and (iii) the larger surface area provides abundant active sites for the reaction, and the high porosity increases its wettability as confirmed by contact angle measurement. The normalized HER rate was also calculated to distinguish the effect of surface area as shown in Fig. 6a, where GCN still show higher activity than bulk g-C_3N_4. Thus, the higher activity of oxygen doped porous g-C_3N_4 does not only base on high surface area, it is also enhanced due to the modification of electronic structure that improves the inherent charge separation and light harvesting abilities.

4. Conclusions

We report the synthesis of highly effective oxygen-doped porous g-C_3N_4 photocatalyst for efficient photocatalytic hydrogen production through the formation of homogeneous supramolecular complexes by hydrothermal process in water. The homogeneous supramolecular assembly ensures sufficient incorporation between melamine and its hydrolysis product cyanuric acid, which provides well-ordered in-plane supramolecular precursor for uniform nanoporous and O-doping C_3N_4 3D networks. This method simultaneously introduces porous structure and heteroatom (oxygen) doping in g-C_3N_4 to tune its active sites and electronic structure for enhanced light-harvesting, wettability, charge separation and transfer. The resulted g-C_3N_4 catalysts bears enhanced hydrogen evolution activity by a factor of 11.3 (with apparent quantum efficiency of 10.3% at 420 nm) compared to bulk g-C_3N_4. The simultaneous designing of porous structure and heteroatom doping through the formation of homogenous supramolecular complex by efficient and ecofriendly hydrothermal process will provide a pathway in developing new photocatalysts for visible-light-driven hydrogen production.

Acknowledgements

The authors appreciate the support from the National Natural Science Foundation of China (21676193, 51661145026, 21506156), the Tianjin Municipal Natural Science Foundation (15JCZDJC37300, 16JCQNJC05200) and Pakistan Science Foundation PSF/257 NSFC-Eng/P-UOL(02).

Appendix A. Supplementary data

Supplementary data associated with this article can be found, in the online version, at http://dx.doi.org/10.1016/j.apcatb.2017.09.003.

References

[1] W.J. Ong, L.L. Tan, Y.H. Ng, S.T. Yong, & S. P. Chai, Graphitic carbon nitride (g-C_3N_4)-based photocatalysts for artificial photosynthesis and environmental remediation: are we a step closer to achieving sustainability? Chem. Rev. 116 (2016) 7159–7329.
[2] X.C. Wang, K. Maeda, A. Thomas, K. Takanabe, G. Xin, J.M. Carlsson, K. Domen, M. Antonietti, A metal-free polymeric photocatalyst for hydrogen production from water under visible light, Nat. Mater. 8 (2009) 76–80.
[3] M. Tahir, N. Mahmood, L. Pan, Z.-F. Huang, Z. Lv, J. Zhang, F.K. Butt, G. Shen, X. Zhang, S.X. Dou, J.-J. Zou, Efficient water oxidation through strongly coupled graphitic C_3N_4 coated cobalt hydroxide nanowires, J. Mater. Chem. A 4 (2016) 12940–12946.
[4] C. Ye, J.X. Li, Z.J. Li, X.B. Li, X.B. Fan, L.P. Zhang, B. Chen, C.H. Tung, L.Z. Wu, Enhanced driving force and charge separation efficiency of protonated g-C_3N_4 for photocatalytic O_2 evolution, ACS Catal. 5 (2015) 6973–6979.
[5] S.W. Zhang, J.X. Li, X.K. Wang, Y.S. Huang, M.Y. Zeng, J.Z. Xu, Rationally designed 1D Ag@$AgVO_3$ nanowire/graphene/protonated g-C_3N_4 nanosheet heterojunctions for enhanced photocatalysis *via* electrostatic self-assembly and photochemical reduction methods, J. Mater. Chem. A 3 (2015) 10119–10126.
[6] D.J. Martin, K. Qiu, S.A. Shevlin, A.D. Handoko, X. Chen, Z. Guo, J. Tang, Highly efficient photocatalytic H_2 evolution from water using visible light and structure-controlled graphitic carbon nitride, Angew. Chem. Int. Ed. 53 (2014) 9240–9245.
[7] Z. Wang, W. Guan, Y. Sun, F. Dong, Y. Zhou, W. Ho, Water-assisted production of honeycomb-like g-C_3N_4 with ultralong carrier lifetime and outstanding photocatalytic activity, Nanoscale 7 (2015) 2471–2479.

[8] F. He, G. Chen, Y. Zhou, Y. Yu, Y. Zheng, S. Hao, The facile synthesis of mesoporous g-C_3N_4 with highly enhanced photocatalytic H_2 evolution performance, Chem. Commun. 51 (2015) 16244–16246.
[9] F. He, G. Chen, Y. Yu, Y. Zhou, Y. Zheng, S. Hao, The sulfur-bubble template-mediated synthesis of uniform porous g-C_3N_4 with superior photocatalytic performance, Chem. Commun. 51 (2015) 425–427.
[10] K.S. Lakhi, D.H. Park, K. Al-Bahily, W. Cha, B. Viswanathan, J.H. Choy, A. Vinu, Mesoporous carbon nitrides: synthesis, functionalization, and applications, Chem. Soc. Rev. 46 (2017) 72–101.
[11] J. Liu, H.Q. Wang, Z.P. Chen, H. Moehwald, S. Fiechter, R. van de Krol, L.P. Wen L. Jiang, M., Antonietti, Microcontact-printing-assisted access of graphitic carbon nitride films with favorable textures toward photoelectrochemical application, Adv. Mater. 27 (2015) 712–718.
[12] K. Kailasam, J.D. Epping, A. Thomas, S. Losse, H. Junge, Mesoporous carbon nitride-silica composites by a combined sol-gel/thermal condensation approach and their application as photocatalysts, Energy. Environ. Sci 4 (2011) 4668–4674.
[13] H.J. Yan, Soft-templating synthesis of mesoporous graphitic carbon nitride with enhanced photocatalytic H_2 evolution under visible light, Chem. Commun. 48 (2012) 3430–3432.
[14] Z. Yang, Y. Zhang, Z. Schnepp, Soft and hard templating of graphitic carbon nitride, J. Mater. Chem. A 3 (2015) 14081–14092.
[15] J. Xu, Y.J. Wang, Y.F. Zhu, Nanoporous graphitic carbon nitride with enhanced photocatalytic performance, Langmuir 29 (2013) 10566.
[16] M. Dhiman, B. Chalke, V. Polshettiwar, Efficient synthesis of monodisperse metal (Rh, Ru Pd) nanoparticles supported on fibrous nanosilica (KCC-1) for catalysis, ACS Sustain. Chem. Eng. 3 (2015) 3224–3230.
[17] A. Fihri, M. Bouhrara, U. Patil, D. Cha, Y. Saih, V. Polshettiwar, Fibrous nano-silica supported ruthenium (KCC-1/Ru): A sustainable catalyst for the hydrogenolysis of alkanes with good catalytic activity and lifetime, ACS Catal. 2 (2012) 1425–1431.
[18] V. Polshettiwar, D. Cha, X. Zhang, J.M. Basset, High-surface-area silica nanospheres (KCC-1) with a fibrous morphology, Angew. Chem. Int. Ed. 49 (2010) 9652–9656.
[19] F. Goettmann, A. Fischer, M. Antonietti, A. Thomas, Chemical synthesis of mesoporous carbon nitrides using hard templates and their use as a metal-free catalyst for Friedel-Crafts reaction of benzene, Angew. Chem. Int. Ed. 45 (2006) 4467–4471.
[20] M. Shalom, M. Guttentag, C. Fettkenhauer, S. Inal, D. Neher, A. Llobet, M. Antonietti, In situ formation of heterojunctions in modified graphitic carbon nitride: synthesis and noble metal free photocatalysis, Chem. Mater. 26 (2014) 5812–5818.
[21] Y. Jun, J. Park, S. Lee, A. Thomas, W. Hong, G. Stucky, Three-dimensional macroscopic assemblies of low-dimensional carbon nitrides for enhanced hydrogen evolution, Angew. Chem. Int. Ed. 52 (2013) 11083–11087.
[22] M. Shalom, S. Gimenez, F. Schipper, I. Herraiz-Cardona, J. Bisquert, M. Antonietti, Controlled carbon nitride growth on surfaces for hydrogen evolution electrodes, Angew. Chem. Int. Ed. 53 (2014) 3654–3658.
[23] Z.P. Chen, M. Antonietti, D. Dontsova, Enhancement of the photocatalytic activity of carbon nitrides by complex templating, Chem. Eur. J. 21 (2015) 10805–10811.
[24] T. Jordan, N. Fechler, J. Xu, T.J.K. Brenner, M. Antonietti, M. Shalom, Caffeine doping of carbon/nitrogen-based organic catalysts: caffeine as a supramolecular edge modifier for the synthesis of photoactive carbon nitride tubes, ChemCatChem 7 (2015) 2826–2830.
[25] M. Shalom, S. Inal, C. Fettkenhauer, D. Neher, M. Antonietti, Improving carbon nitride photocatalysis by supramolecular preorganization of monomers, J. Am. Chem. Soc. 135 (2013) 7118–7121.
[26] E.E. Simanek, M. Mammen, D.M. Gordon, D.N. Chin, J.P. Mathias, C.T. Seto, G.M. Whitesides, Design and synthesis of hydrogen-bonded aggregates: theory and computation applied to three systems based on the cyanuric acid-melamine lattice, Tetrahedron 51 (1995) 607–619.
[27] Y.-S. Jun, E.Z. Lee, X. Wang, W.H. Hong, G.D. Stucky, A. Thomas, From melamine-cyanuric acid supramolecular aggregates to carbon nitride hollow spheres, Adv. Funct. Mater. 23 (2013) 3661–3667.
[28] L.Q. Yang, J.F. Huang, L. Shi, L.Y. Cao, Q. Yu, Y.N. Jie, J. Fei, H.B. Ouyang, J.H. Ye, A surface modification resultant thermally oxidized porous g-C_3N_4 with enhanced photocatalytic hydrogen production, Appl. Catal. B: Environ. 204 (2017) 335–345.
[29] Z.-F. Huang, J.J. Song, L. Pan, Z. Wang, X.Q. Zhang, J.-J. Zou, W.B. Mi, X.W. Zhang, L. Wang, Carbon nitride with simultaneous porous network and O-doping for efficient solar-energy-driven hydrogen evolution, Nano Energy 12 (2015) 646–656.
[30] L. Ming, H. Yue, L. Xu, F. Chen, Hydrothermal synthesis of oxidized g-C_3N_4 and its regulation of photocatalytic activity, J. Mater. Chem. A 2 (2014) 19145–19149.
[31] J. Li, B. Shen, Z. Hong, B. Lin, B. Gao, Y. Chen, A facile approach to synthesize novel oxygen-doped g-C_3N_4 with superior visible-light photoreactivity, Chem. Commun. 48 (2012) 12017–12019.
[32] G.H. Dong, Z.H. Ai, L.Z. Zhang, Efficient anoxic pollutant removal with oxygen functionalized graphitic carbon nitride under visible light, RSC Adv. 4 (2014) 5553–5560.
[33] J. Liu, W. Li, L. Duan, X. Li, L. Ji, Z. Geng, K. Huang, L. Lu, L. Zhou, Z. Liu, W. Chen, L. Liu, S. Feng, Y. Zhang, A graphene-like oxygenated carbon nitride material for improved cycle-life lithium/sulfur batteries, Nano Lett. 15 (2015) 5137–5142.
[34] S. Liu, D. Li, H. Sun, H.M. Ang, M.O. Tade, S. Wang, Oxygen functional groups in graphitic carbon nitride for enhanced photocatalysis, J. Colloid Interface Sci. 468 (2016) 176–182.
[35] Y. Wang, X. Wang, M. Antonietti, Polymeric graphitic carbon nitride as a heterogeneous organocatalyst: from photochemistry to multipurpose catalysis to sustainable chemistry, Angew. Chem. Int. Ed. 51 (2012) 68–89.
[36] Y. Ishida, L. Chabanne, M. Antonietti, M. Shalom, Morphology control and photocatalysis enhancement by the one-pot synthesis of carbon nitride from preorganized hydrogen-bonded supramolecular precursors, Langmuir 30 (2014) 447–451.
[37] S.J. Makowski, P. Köstler, W. Schnick, Formation of a hydrogen-bonded heptazine framework by self-assembly of melamine into a hexagonal channel structure, Chem. Eur. J. 18 (2012) 3248–3257.
[38] Y. Wang, M.K. Bayazit, S.A. Moniz, Q. Ruan, C.C. Lau, N. Martsinovich, J. Tang, Linker-controlled polymeric photocatalyst for highly efficient hydrogen evolution from water, Energy Environ. Sci 10 (2017) 1643–1651.
[39] S. Guo, Z. Deng, M. Li, B. Jiang, C. Tian, Q. Pan, H. Fu, Phosphorus-doped carbon nitride tubes with a layered micro-nanostructure for enhanced visible-light photocatalytic hydrogen evolution, Angew. Chem. 55 (2016) 1830–1834.
[40] G. Liu, P. Niu, C.H. Sun, S.C. Smith, Z.G. Chen, G.Q. Lu, H.M. Cheng, Unique electronic structure induced high photoreactivity of sulfur-doped graphitic C_3N_4, J. Am. Chem. Soc. 132 (2010) 11642–11648.
[41] Z. Chen, A. Savateev, S. Pronkin, V. Papaefthimiou, C. Wolff, M.G. Willinger, E. Willinger, D. Neher, M. Antonietti, D. Dontsova, The Easier the Better preparation of efficient photocatalysts-metastable poly(heptazine imide) salts, Adv. Mater. (2017), http://dx.doi.org/10.1002/adma.201700555.
[42] V.W. Lau, V.W. Yu, F. Ehrat, T. Botari, I. Moudrakovski, T. Simon, V. Duppel, E. Medina, J.K. Stolarczyk, J. Feldmann, V. Blum, B.V. Lotsch, Urea-modified carbon nitrides: enhancing photocatalytic hydrogen evolution by rational defect engineering, Adv. Energy Mater. (2017), http://dx.doi.org/10.1002/aenm.201602251.
[43] L. Pan, S. Wang, J. Xie, L. Wang, X. Zhang, J.-J. Zou, Constructing TiO_2 p-n homojunction for photoelectrochemical and photocatalytic hydrogen generation, Nano Energy 28 (2016) 296–303.
[44] L. Pan, S. Wang, W. Mi, J. Song, J.-J. Zou, L. Wang, X. Zhang, Undoped ZnO abundant with metal vacancies, Nano Energy 9 (2014) 71–79.
[45] X. Jia, M. Tahir, L. Pan, Z.-F. Huang, X. Zhang, L. Wang, J.-J. Zou, Direct Z-scheme composite of CdS and oxygen-defected $CdWO_4$: an efficient visible-light-driven photocatalyst for hydrogen evolution, Appl. Catal. B 198 (2016) 154–161.